



City Research Online

City, University of London Institutional Repository

Citation: Weng, Y., Qian, K., Fu, F. & Fang, Q. (2020). Numerical Investigation on Load Redistribution Capacity of Flat Slab Substructures to Resist Progressive Collapse. *Journal of Building Engineering*, 29, 101109. doi: 10.1016/j.jobe.2019.101109

This is the accepted version of the paper.

This version of the publication may differ from the final published version.

Permanent repository link: <https://openaccess.city.ac.uk/id/eprint/23393/>

Link to published version: <https://doi.org/10.1016/j.jobe.2019.101109>

Copyright: City Research Online aims to make research outputs of City, University of London available to a wider audience. Copyright and Moral Rights remain with the author(s) and/or copyright holders. URLs from City Research Online may be freely distributed and linked to.

Reuse: Copies of full items can be used for personal research or study, educational, or not-for-profit purposes without prior permission or charge. Provided that the authors, title and full bibliographic details are credited, a hyperlink and/or URL is given for the original metadata page and the content is not changed in any way.

City Research Online:

<http://openaccess.city.ac.uk/>

publications@city.ac.uk

Numerical Investigation on Load Redistribution Capacity of Flat Slab

Substructures to Resist Progressive Collapse

Yun-Hao Weng¹, Kai Qian^{1*}, Feng Fu², and Qin Fang³

¹ College of Civil Engineering and Architecture, Guangxi University, 100 Daxue Road, China, 530004.

² School of Mathematics, Computer Science and Engineering, City, University of London, London, EC1V 0HB UK

³ Army Engineering University, Nanjing 210007, Jiangsu, Peoples R China

Abstract: To study the load redistribution capacity of reinforced concrete (RC) flat slab structures subjected to a middle column loss scenario, high fidelity finite element (FE) models were built using commercial software LS-DYNA. The numerical models were validated by experimental results. It is found that the continuous surface cap model (CSCM) with an erosion criterion considering both the maximum principal and shear strain could effectively predict the punching shear failure at slab-column connections. The validated FE models were employed to investigate the effect of boundary conditions, amount of integrity reinforcement, and slab thickness on the load redistribution capacity of flat slab structures. Furthermore, multi-story RC flat slab substructures were built to capture the load redistribution behavior of different floors. Parametric studies indicate that ignoring the constraints from surrounding slabs may underestimate the load redistribution capacity of the flat slab substructures. Therefore, it is suggested that in future numerical or experimental studies, rigid horizontal constraints should be applied at the slab edge of the substructure to well represent the constraints from surrounding slabs. In addition, it is also found that the amount of integrity reinforcement would significantly affect the post-punching performance of flat slab structures. It is suggested that the minimum integrity reinforcement ratio should be 0.63 %.

Keywords: Progressive collapse; Flat slab substructures; Quasi-static; Punching shear; Load resisting mechanism

* Corresponding author. Tel.: 65+67905292, E-mail address: qiankai@gxu.edu.cn

26 **1. Introduction**

27 An initial local failure of supporting components due to accidents may lead to a disproportionate
28 collapse of the structure, which is defined as disproportionate collapse or progressive collapse. The
29 consequence of casualties caused by progressive collapse event is very tragic. Progressive collapse
30 attracted public attention first after the collapse of Ronan Point apartment in 1968 and raised
31 concerns by design regulators after the catastrophic consequences of the Murrah Federal Building in
32 Oklahoma City in 1995 and World Trade Centre in New York City in 2001. Several design
33 guidelines (DoD 2009 [1]; GSA 2003 [2]; ASCE/SEI-10 2010 [3]; COST Action TU0601 2008 [4])
34 were proposed accordingly. Moreover, these progressive collapse incidents also attracted a large
35 number of researchers to investigate the load redistribution behavior and load resisting mechanisms
36 of the structures subjected to different column removal scenarios. In the past decade, several studies
37 have been conducted to study progressive collapse based on the alternative load path method
38 stipulated in DoD [1] and GSA [2].

39 Su et al. [5] tested twelve reduced-scale RC beam-column sub-assemblages to investigate the
40 effects of beam reinforcement ratio, span-to-depth ratio, and loading rate on the compressive arch
41 action of RC frames. Two one-half scaled sub-assemblages with seismic and non-seismic detailing
42 were tested by Yu and Tan [6] to evaluate the effects of seismic design on behavior of RC frames in
43 resisting progressive collapse. Feng et al. [7] evaluated the behavior of precast concrete structures to
44 resist progressive collapse by using a three-dimensional FE model. Fascetti et al. [8] proposed a
45 procedure to evaluate the robustness of RC frame against progressive collapse based on a macro-
46 model simulation. Livingston et al. [9] carried out a series of pushdown analysis to quantify the
47 effects of structural characteristics (e.g. axial stiffness at the beam boundaries, amount of integrity
48 reinforcement at bar cut-off locations, etc) on progressive collapse resistance of frames. High fidelity
49 solid-element-based numerical models were used by Yu et al. [10] to investigate the robustness of
50 RC beam-slab substructures under perimeter column removal scenarios. Shan et al. [11] tested two
51 one-third scale, four-bay by two-story RC frame to investigate the effects of infilled wall on the load
52 resisting mechanisms of RC frames. Based on their tests, it was concluded that infilled walls could

53 enhance the load resisting capacity of RC frames significantly due to more alternative load paths
54 provided. However, the infilled walls might decrease the ductility of the frames. Sadek et al. [12]
55 tested four (two RC and two steel) full-scale beam-column sub-assemblages subjected to the loss of
56 an interior column to provide insight into the mobilization of catenary action. Qian and Li [13] tested
57 two series of six specimens (with and/or without RC slab) to quantify the contribution of RC slabs in
58 resisting progressive collapse under a corner column loss scenario. It was found that RC slabs could
59 improve the ultimate load resisting capacity by 63 %. Pham et al. [14] investigated the effect of
60 different loading patterns and boundary conditions on tensile membrane action (TMA) of beam-slab
61 systems. Lu et al. [15] and Ren et al. [16] conducted a number of one-third scaled specimens to
62 investigate the effects of RC slabs on the behavior of RC frames to resist progressive collapse caused
63 by either an edge or an interior column loss scenario. Feng et al. [17] used the probability density
64 evolution method to evaluate the robustness of RC beam-column sub-assemblage under a column
65 missing scenario.

66 Flat slab floor system has been widely used in tall and multi-story buildings, due to its long span
67 and small thickness features. However, there is relatively little attention paid on flat slab structures to
68 resist progressive collapse. For flat slab structures, a column loss leads to load redistribution, result in
69 the increase of bending moment and shear force at adjacent slab-column connections significantly.
70 The likelihood of progressive collapse increases as no load redistribution in beams can be triggered in
71 flat slab structures. This may cause collapse of the buildings such as of the incidents of Sampoong
72 Department Store at Seoul, South Korea. Russell et al. [18] tested seven 1/3 scaled RC flat slab
73 substructures subjected to the quasi-static or dynamic loading regimes. The experimental results
74 showed that flat slabs could redistribute the loads effectively after a column lost. However, punching
75 shear failure was a critical issue must be addressed seriously. Qian and Li [19, 20] and Ma et al. [21]
76 conducted several series of tests to investigate the load resisting mechanisms and quasi-static
77 behaviour of RC flat slab structures subjected to the loss of corner or interior column scenarios.
78 Keyvani et al. [22] developed a new finite element modeling technique to simulate punching and
79 post-punching behavior of flat plates. Moreover, the effects of compressive membrane action (CMA)

80 on load resisting capacity of flat plate structures were also investigated by Keyvani et al. [22]. Liu et
81 al. [23] proposed a macromodel for slab-column connections, which could be used to simulate the
82 behaviour of flat slab or flat plate structures in resisting progressive collapse. Peng et al. [24] carried
83 out a series of dynamic tests to study the dynamic response of flat plate substructure subjected to
84 instantaneously removal of an exterior column. Qian et al. [25] conducted experimental and
85 numerical studies to evaluate the dynamic response of flat slab structures subjected to different
86 extents of initial local damage (one-column or two-column removal).

87 Due to the complexity of testing on multi-panel flat slab structures, the majority of existing
88 experimental tests on progressive collapse resistance are single-storey substructures or sub-
89 assemblages with simplified boundary condition (applying weights at the overhang to simulate the
90 constraints from surrounding components [19-21, 24] or ignoring the constraints from surrounding
91 components [18]), which is different from the real conditions in a building. It is necessary to conduct
92 further studies to evaluate the effects of boundary condition on the behavior of flat slab substructures
93 to mitigate progressive collapse. Moreover, due to excessive time and high cost for experimental
94 studies, some of critical parameters could not be investigated by experimental studies. Therefore,
95 developing an accurate numerical simulation method is imperative. In this paper, numerical
96 simulation based on high fidelity FE models are developed using LS-DYNA. The FE models are
97 validated by test results. Then, the validated FE models are used to quantify the effect of surrounding
98 slabs and upper floors on the load redistribution capacity of flat slab substructure. In addition, for
99 multi-storey flat slab buildings, the load redistribution ability of each floor was evaluated
100 individually to reveal the difference of loading resisting mechanisms and load resisting contribution
101 of each floor. Finally, the effects of integrity reinforcement and slab thickness on the load
102 redistribution capacity of flat slab substructures are also investigated.

103 2. Experimental program and numerical validation

104 2.1. Brief of experimental program

105 To determine the possible load resisting mechanisms in flat slab structures to resist progressive
106 collapse, a test program was conducted by Qian and Li [20]. An experimental program included three
107 1/4 scaled multi-panel flat slab substructures. The prototype of these specimens was designed
108 according to provisions of ACI 318-11 [26]. The total dead load (DL) including the self-weight of the
109 slab and the weights of infilled walls was assumed to be 8.0 kPa. The live load (LL) was assumed to
110 be 3.0 kPa. Two specimens (ND and WD) from Qian and Li [20] are used to validate numerical
111 models. These two flat slab substructures have identical dimensions and reinforcement details. One
112 of the specimens has enhanced punching shear capacity due to the drop panels at slab-column
113 connections. Table 1 gives the specimen properties while Fig. 1 shows the dimensions and
114 reinforcement details of Specimen WD. As it can be seen from the figure, Specimen WD consists of
115 a slab with dimension of 3750 mm×3750 mm×55 mm, nine columns including one interior column
116 and eight surrounding columns, and nine drop panels with size of 450 mm×450 mm×35 mm. The
117 cross-section of columns was 200 mm×200 mm. The interior column was reinforced by 4-T13.
118 However, the surrounding columns were reinforced by 8-T13 to further enhance their strength and
119 stiffness. The drop panel was reinforced with a single layer mesh of R6@80 mm. The RC flat slab
120 was reinforced using two layers of R6@250 mm mesh. Moreover, in the bottom layer, integrity rebar
121 of 3R6 was installed within the column reinforcing cage in orthogonal directions, to meet the
122 detailing requirements of ACI 381-11 [26] (more than two reinforcements passing through the
123 column cage as integrity rebar). T13 and R6 represent the deformed rebar with diameter of 13 mm
124 and plain rebar with diameter of 6 mm, respectively. The yield strength and ultimate strength of R6
125 were 500 MPa and 617 MPa, and those of T13 were 529 MPa and 608 MPa. After 28 days curing,
126 the measured concrete compressive strength of Specimens ND and WD was 22.5 MPa and 22.3 MPa,
127 respectively.

128 Test setup and instrumentation layout of Specimen WD are shown in Fig. 2. As shown in the
129 figure, the specimen was supported by eight steel legs. A special load distribution rig was designed to
130 equivalently replicate the uniform distributed load (UDL). The detailing of the load distributed rig is
131 illustrated in Fig. 3. It has three rigid beams, four triangle steel plates, and twelve small steel plates.
132 Between the secondary steel beams and triangle steel plates, hemisphere balls and socket joints were
133 utilized to ensure the load can be vertically applied during the tests, even at the stage that the large
134 deformation of slabs. Moreover, a hydraulic jack with a stroke of 600 mm was utilized to apply loads
135 and a steel assembly (Item 4 in Figure 2) was designed to ensure that the applied load keeps
136 vertically. More details about the test program please refer to Qian and Li [20].

137 *2.2. Details of numerical model*

138 In this study, high fidelity finite element model was developed to investigate the difference of
139 load resisting mechanisms on each floor of a multi-storey flat slab structure subjected to a middle
140 column removal scenario. The explicit software LS-DYNA [27] was employed due to its numerical
141 stability and sufficient availability of constitutive models. Although quasi-static behavior of the flat
142 slab substructure was focused on in this study, explicit solver was adopted to avoid divergence
143 problem at large deformation stage.

144 *2.2.1 Element type*

145 Fig. 4 shows the geometrical model of WD. For another model ND, it is identical to WD in
146 slabs, columns, and reinforcement details, except no drop panels are modelled. To simulate the
147 boundary conditions more close to real test conditions, eight steel legs and the load distribution rig
148 were also simulated in FE modeling. The element of concrete adopted in this study is 8-node solid
149 elements with reduced integration. This reduced integration element can save computational time on
150 the premise of accuracy when hourglass control is well defined. To ensure the hourglass energy was
151 less than 10 % of the total internal energy, Flanagan-Belytschko stiffness form with exact volume
152 integration was used for solid elements. Thus, the hourglass coefficient was defined as 0.002. A 2-
153 node Hughes-Liu beam element with 2×2 Gauss quadrature integration was employed to simulate the

154 reinforcements. This Hughes-Liu beam element could effectively simulate the mechanical behavior
155 of reinforcement bars, such as axial force, bi-axial bending, and transverse shear. Moreover, the load
156 distribution rig and steel supports were also modeled by explicit solid element.

157 For the connection between reinforcement and concrete, previous studies [10, 14] had proved
158 that the assumption of perfect bonding between slab reinforcement and concrete could ensure enough
159 accuracy to simulate the behavior of RC component subjected to a column removal scenario. As a
160 result, perfect bonding between concrete and reinforcement was assumed by keyword
161 *Constrained_Lagrange_In_Solid in this study.

162 2.2.2 Boundary conditions and loading method

163 The RC slab was fixed onto the steel legs with shared nodes in the interface, as shown in Fig. 4.
164 To ensure the beam elements and the concrete elements work together, the nodes at the end of
165 longitudinal reinforcements of RC columns were tied to the steel plates by using keyword
166 *Contact_Tied_Nodes_To_Surface. Fixed boundary conditions were applied at the bottom of the
167 steel supports. Moreover, eight steel plates were modeled to apply the steel weights (Item 7 in Figure
168 2) as used in the reference test [20], as shown in Fig. 4. Steel plates were fixed to RC slab with
169 contact surface using keyword *Contact_Automatic_Surface_To_Surface (*CASTS).

170 As shown in Fig. 5, the load distribution rig from Qian and Li [20] is simulated with high
171 fidelity. It contains a series of rigid beams and plates. The top rigid beams were connected with the
172 secondary rigid beam by revolute joints defined by keyword *Constrained_Joint_Revolute. The
173 secondary rigid beam was connected with the triangle rigid plates by spherical joints defined by
174 keyword *Constrained_Joint_Spherical. Revolute joints were defined between bottom small steel
175 plates and the triangle steel plates to ensure the small plates were able to rotate around the revolute
176 joints. Furthermore, single surface (*Contact_Automatic_Single_Surface) was defined between the
177 load distribution rig and RC slab.

178 As shown in Fig. 5, a rigid plate with only vertical freedom was built on the middle of the first
179 rigid beam to apply load on the slab. *CASTS were defined between the bottom surface of the rigid

180 plate and the top surface of the first rigid beam. The vertical load from the hydraulic jack in the test
181 program [20] was simulated by applying a velocity-time history for the rigid plate on the middle of
182 the first rigid beam. The velocity increases from 0 mm/ms under a small constant acceleration at the
183 beginning to avoid severe vibration of structural resistance, as suggested by the works [10, 28], and
184 then stays constant. The maximum velocity and acceleration were set to 0.2 mm/ms and 6.7×10^{-4}
185 mm/ms², respectively, by a sensitivity analysis based on Specimen ND.

186 2.2.3 Material model

187 In this study, continuous surface cap model (CSCM) was chosen to simulate the concrete
188 properties, as several studies have proven its accuracy to simulate quasi-static behavior of RC
189 components subjected to column removal scenarios [10, 14, 28, 29]. The CSCM can effectively
190 simulate the material properties of concrete (such as damage-based softening and modulus reduction,
191 shear dilation, shear compaction, confinement effect, and strain rate effect, etc.) under low
192 confinement situations [30]. Its yield surface consists of shear failure surface and hardening cap
193 surface [27], as shown in Fig. 6. The original CSCM (*Mat_CSCM) requires a series of input
194 parameters to define concrete material properties. LS-DYNA also provides a simplified CSCM
195 (*Mat_CSCM_CONCRETE) for concrete properties with unconfined compressive strength between
196 28 MPa and 48 MPa. The simplified CSCM only needs three input parameters (unconfined
197 compressive strength f_c , maximum aggregate size A_g , and units), and then the remaining material
198 properties are calculated automatically according to equations proposed by CEB-FIP concrete model
199 code [31]. The unconfined compressive strength f_c' of Specimens ND and WD was 22.5 MPa and
200 22.3 MPa, respectively. For simplicity, the average value 22.4 MPa was applied in the numerical
201 models. The maximum aggregate size A_g is 10 mm. However, the default concrete material properties
202 would over-predict the structural resistances of FE models. Therefore, concrete material properties
203 were made a few adjustments on the fracture energy. Previous studies [10, 28] suggest that the tensile
204 fracture energy G_{ft} could take 80 % of the default one when it is over-prediction, and the shear
205 fracture energy G_{fs} should be reduced as $G_{fs} = 50G_{ft}$ (The default is $G_{fs} = 100G_{ft}$) when shear damage is

206 evident. Both G_{ft} and G_{fs} are adjusted, as severe punching shear failure occurred in Specimen ND.
207 The detailed parameters of CSCM are tabulated in Table 2. The unconfined uniaxial stress-strain
208 relationship of concrete after adjustments is shown in Fig. 7. The CSCM also provides an erosion
209 algorithm based on maximum principal strain to simulate material failure. If the maximum principal
210 strain of concrete element is greater than the failure principal strain the concrete element will be
211 deleted. Although element erosion has little physical meaning, several studies [10, 14, 28, 29] found
212 that erosion criterion based on the maximum principal strain is a suitable way to simulate concrete
213 failure under quasi-static condition. However, it will be very hard to simulate the shear failure of
214 concrete if only the maximum principal strain criterion was used to define the erosion of concrete
215 element. Thus, the maximum principal strain and shear strain criteria were taken into consideration
216 in this study by using keyword *Mat_Add_Erosion. Since the appropriate values are dependent on
217 mesh size, the values of principal strain and shear strain at failure were final set to 0.1 and 0.08,
218 respectively, by many times of trial calculation based on Specimen ND. Furthermore, the strain rate
219 effect was ignored since only quasi-static behavior was discussed in this study.

220 The isotropic elastic-plastic material model (*Mat_Plastic_Kinematic) was chosen for
221 reinforcement. The parameters of material properties, including elastic modulus, yield strength,
222 tangential modulus, and ultimate strain, were determined in accordance with the material tests. In
223 addition, the strain rate effect was also ignored.

224 Sensitivity analysis was conducted with three mesh sizes, as listed in Table 3. As shown in Fig.
225 8, Mesh 2 is reasonable for Specimen ND, as further mesh refinement cannot lead to any remarkable
226 convergence but instead taking more computing time. Therefore, the mesh size of concrete element
227 was 18.33 mm×25 mm×25 mm for RC slab and 25 mm×25 mm×25 mm for other components. The
228 size of beam element was 30 mm.

229 *2.3 Validation by test results*

230 Fig. 9 shows the comparison of load-displacement curves from FE simulation and experimental
231 tests. For Specimen ND, as shown in Fig. 9(a), after reaching the yield load, the load resistance

232 decreased due to secondary punching shear failure, which agrees with the experimental observation
233 well. For Specimen WD, as shown in Fig. 9(b), the load resistance decreased slowly after reaching
234 the first peak load (FPL), indicating its failure was mainly controlled by flexural failure, which was
235 similar to that of test results. The error of key results between the FE models and test specimens is
236 less than 10 %, as listed in Table 4. Therefore, the proposed FE models could effectively simulate the
237 behavior of punching shear failure and the effectiveness of drop panels.

238 It should be noted that the concrete damage was expressed by the damage index. Damage
239 index of 0 and 1 represents no damage and completed failure, respectively. As shown in Figs. 10 and
240 11, FE model could simulate the crack pattern of tested specimen well. For Specimen ND, FE model
241 could predict the punching shear failure of the slab-column connection well, as shown in Fig. 12. As
242 shown in Fig. 13, the failure mode of Specimen WD could also be well simulated. As a result, the FE
243 models could be used for further parametric study.

244 **3. Effects of boundary condition simplification**

245 For both specimens, due to the limitation of cost and space, only substructures (two-bay by
246 two-bay) were tested. However, in reality, the remaining parts of the building (such as the
247 surrounding slabs and upper floors) may affect the response of the substructures significantly, which
248 was ignored in experimental program. As a result, in this section, the validated FE models were
249 utilized to quantify the effects of boundary condition simplification.

250 *3.1. Effects of surrounding slabs*

251 Around the substructure, the surrounding slabs will provide certain constraints (rotational,
252 horizontal, or vertical constraints). However, for Specimens WD and ND, the constraints from
253 surrounding slabs were simulated by applying service pressure at the overhang, which is one-quarter
254 of column spacing. Previous works [25] found that the simplified boundary may underestimate the
255 constraints from surrounding slabs. Thus, to further understand the discrepancy between the
256 simplified boundaries and realistic boundaries, four numerical models with different constraints at the
257 overhang (refer to Fig. 14) and one numerical model with four-bay by four-bay (refer to Fig. 15)

258 were developed based on the validated FE model for Specimen ND. As shown in Fig. 14, ND-P, ND-
259 H, ND-V, and ND-F represent ND with design gravity loads (live and dead) at the overhang, with
260 rigid horizontal constraint applied at the overhang edge, with rigid vertical constraint applied at the
261 overhang edge, full constraints (rotational, horizontal, and vertical constraints) applied at the
262 overhang edge, respectively. It should be noted that the design gravity load (live and dead) was also
263 applied at the overhang of ND-H, ND-V, and ND-F. Moreover, as shown in Fig. 15, ND-R was
264 modelled in four-bay by four-bay to include the effects of surrounding slabs realistically. Similarly,
265 for ND-R, the design gravity load (live and dead) was also applied at the surrounding slabs.

266 Fig. 16 compares the load-displacement curves of ND with varying constraints. The load
267 resistances of ND-P and ND-V are exactly same but lower than that of ND-R, indicating that the
268 simplified boundary condition for tested specimens underestimates the constraints from surrounding
269 bay. In addition, the rigid vertical constraint at the overhang edge has little effects on the load
270 resistance. Conversely, ND-F with full constraints at the overhang edge (model ND-F) achieves
271 higher load resistance than that of ND-R. Similar conclusion was obtained by Peng et al. [32].
272 However, the load resistance of model ND-H is very close to that of ND-R. The comparison of ND-H
273 and ND-F indicates that the rotational restraint at the overhang edge could further increase the load
274 resistance. Thus, to achieve more realistic structural response, only rigid horizontal constraints should
275 be applied at the slab edge.

276 3.2. Effects of upper floors

277 Only single-story flat slab substructures were tested in the test program [20]. However,
278 progressive collapse is a global behavior. Thus, it is necessary to investigate the response of multi-
279 story flat slab structure. As shown in Fig.17, ND-1F, ND-2F, and ND-3F represent single-story, two-
280 story, and three-story flat slab substructure, respectively. The dimension, reinforcement details, and
281 boundary conditions at the overhang edge in each story are identical as those at model ND. The load
282 distribution rig was generated in each story, and identical service load was applied at the overhangs
283 of each story.

284 To be consistent, it should be noted that only the load resistance from the first story of these
285 models was extracted for comparison, as shown in Fig. 18. It can be seen that the load resistance of
286 ND-2F is extremely similar to that of ND-1F. Although ND-3F achieved largest load resistance
287 before occurrence of the secondary punching shear failure, the maximum difference is less than 5 %.
288 As a result, the structural response of the extracted substructure is insensitive to the constraints from
289 the upper stories.

290 *3.3. Combined effects due to surrounding slabs and upper floors*

291 To investigate the combined effect due to surrounding slabs and upper floors, a global FE
292 model ND-3F-R was built based on ND-3F, as shown in Fig. 19. ND-3F-R (four-bay by four-bay but
293 three stories) has similar reinforcement details and dimensions as ND-3F and surrounding slabs were
294 also modelled directly. Design gravity loads (live and dead) were also applied on the surrounding
295 slabs.

296 Fig. 20 shows the comparison of the resistances of the first story between ND-1F and ND-3F-R.
297 As can be seen in the figure, the FPL of ND-3F-R is larger than that of ND-1F by 13.8 %. Note that
298 the FPL of ND-R is larger than that of ND-P by 12.6 % (effect of surrounding slabs while the FPL of
299 ND-3F is larger than that of ND-1F by 1.0 % (effect of upper floors). Therefore, the effects of
300 surrounding slabs and upper floors could be superposed.

301 **4. Load resisting mechanisms of each story for a multi-storey flat slab structure**

302 As aforementioned, progressive collapse is a global behavior for a multi-storey building.
303 However, majority of existing tests in progressive collapse investigation were based on single-storey
304 substructures due to cost and time limitation. These studies are based on the assumption that each
305 story of the structures has identical load resistance and load resisting mechanisms at same
306 deformation stages. However, in reality, above assumption is not true even all floors above the lost
307 column have identical structural components. To evaluate the accuracy of above assumption, the
308 structural response of each story was extracted for comparison based on the models of ND-2F, ND-
309 3F, and ND-3F-R.

310 For ND-2F and ND-3F, as shown in Figs. 21(a) and (b), the structural resistance developing in
311 each story is different. The maximum resistance is observed in the first story. It could be explained
312 that the interaction among different stories, which leads to different in-plane force developed in slab
313 within different stories and mobilization of membrane actions (CMA and TMA). To elaborate on this
314 assumption, the in-plane forces of the slab sections in x direction, as labeled in Fig. 22, were
315 extracted to elucidate the membrane actions developing in flat slab substructure. For simplicity, only
316 the section force of ND-3F was presented. As shown in Fig. 23, the development of the slab-section
317 force in each story is different. In the first story, the section force developing in the slab is in
318 compression (negative) firstly, and then transfers into tension at the large deformation stage.
319 However, the section force of the second story or the third story is always in tension or in
320 compression, respectively. Moreover, the peak value of the section force in the first story is much
321 larger than the ones of other stories. Therefore, for ND-2F and ND-3F, CAA and TMA could develop
322 in the first story effectively, leading to larger resistance. For ND-3F-R, which has a close-to-reality
323 boundary condition, the structural resistance developing in each story is also different. As shown in
324 Fig. 21(c), when the vertical displacement of the middle column is less than 88 mm, the load
325 resistance of the first story is larger than that from the second and third stories.

326 **5. Parametric study**

327 To deeply understand the behavior of flat slab structures to resist progressive collapse, a
328 parametric study was also performed based on the validated FE models.

329 *5.1. Effects of integrity reinforcement*

330 As mentioned above, in the reference tests [20], 3R6 integrity reinforcements were designed
331 passing through the column cages in each principal direction, which was greater than that suggested
332 by ACI 318-11 (2011) [26]. Nevertheless, there was no specific calculation formula for designing of
333 the integrity reinforcement. The arrangement of the integrity reinforcement may affect the load
334 resisting capacity after punching shear failure and deformation capacity of the flat slab structure.
335 Thus, in this section, to quantify the effects of the amount of integrity reinforcement, FE models with

336 different amounts of integrity reinforcement were simulated. Seven different cases (including 0, 1R6,
337 2R6, 3R6, 4R6, 5R6, and 6R6 integrity reinforcements) were considered for ND. Moreover, four
338 different cases (including 0, 1R6, 2R6, and 3R6 integrity reinforcements) were considered for ND-R
339 to investigate the effects of integrity reinforcement under a more real boundary condition. To
340 normalize the amount of integrity reinforcement, integrity reinforcement ratio $\rho_i = A_s/bh_o$ is used. A_s is
341 the total area of the integrity reinforcements; b is the column width (200 mm for these specimens);
342 and h_o is the effective depth of the slab (45 mm for these specimens). Thus, ρ_i of 1R6, 2R6, 3R6, 4R6,
343 5R6 and 6R6 are 0.31 %, 0.63 %, 0.94 %, 1.26 %, 1.57 %, and 1.88 %, respectively.

344 Fig. 24 shows the load-displacement curves of ND with the different amount of integrity
345 reinforcement. The key results are listed in Table 5. As can be seen in the figures and table, with the
346 increase of integrity reinforcement ratio from 0 % to 1.88 % (0 to 6R6), the YL, FPL, and second
347 peak load (SPL) increased by 18.5 %, 41.6 %, and 209.4 %, respectively. It is obvious that increasing
348 the integrity reinforcement ratio can enhance the load resisting capacity at large deformation stage
349 after column removal significantly. This is mainly due to the enhancement of dowel action from
350 integrity reinforcement. However, the efficiency of upgrading the load resisting capacity decreases
351 with increasing the amount of integrity reinforcements. For instance, the YL increases by 15.9 %
352 when the integrity reinforcement ratio increases to 0.94 % (3R6). However, when the integrity
353 reinforcement ratio increases to 1.88 % (6R6), the YL only increases by 18.5 %. Similar phenomenon
354 is observed for the FPL. It is found that when the integrity reinforcement ratio of ND is greater than
355 0.63 % (2R6), the SPL exceeds the FPL. In summary, to have a good post-punching performance of
356 the flat slab structure subjected to the loss of a middle column scenario, the integrity reinforcement
357 ratio is suggested to greater than 0.63 %.

358 Comparing to ND, ND-R may be more prone to failure since extra load from surrounding slabs
359 transfers to the adjacent slab-column connections. As shown in Fig. 25, when there is no integrity
360 reinforcement installed passing through the column cages, the structural resistance of ND-R drops to
361 0 kN suddenly after the secondary punching shear failure occurred. This is because when punching
362 shear failure occurred at one of adjacent slab-column connections, it started to propagate horizontally

363 due to further load redistribution and resulted in total collapse of entire slab, as shown in Fig. 26.
364 Moreover, similar to ND, it can be found that installing 2R6 ($\rho_i=0.63\%$) integrity reinforcements in
365 ND-R can ensure that the SPL (180.2 kN) exceeds the FPL (178.5 kN).

366 5.2. Effects of slab thickness

367 Previous work [19] investigated different slab thickness of RC flat slab structures subjected to
368 the loss of a middle column scenario. However, their specimens were tested under concentrated load.
369 To re-evaluate the effects of slab thickness of RC flat slabs subjected to the loss of a middle column
370 under UDL loading regime, models with slab thickness of 70 mm and 100 mm were simulated based
371 on the validated FE models ND and WD. These models are the same as the validated FE models
372 except the slab thickness.

373 Figs. 27(a) and (b) show the load-displacement curves of WD and ND with different slab
374 thicknesses, respectively. To distinguish, WD with slab thickness of 55 mm, 70 mm, and 100 mm are
375 named WD-55, WD-70, and WD-100, respectively. Similarly, ND-55, ND-70 and ND-100 represent
376 ND with slab thickness of 55 mm, 70 mm, and 100 mm, respectively. As shown in Fig. 27(a), a
377 thicker slab could increase the load resisting capacity significantly. The FPL of WD-100 is larger
378 than that of WD-70 and WD-55 by 65.8 % and 177.1 %, respectively, which is different from the
379 concentrated loading regime in [19]. For WD-70 and WD-100, no obvious re-ascending of load
380 resistance is observed at the large deformation stage after column removal. This is because the
381 residual load-resisting capacity at the large deformation stage is mainly provided by the dowel action
382 from integrity reinforcements and TMA developed in remaining bottom slab reinforcements.
383 However, increasing the slab thickness has little effects on the development of these actions.
384 Moreover, by comparing Fig. 13 with Fig. 28, it is found that the failure modes of WD-100 and WD-
385 70 are quite different to that of WD-55. The main cracks of WD-100 and WD-70 are formed at the
386 edge of column while those of WD-55 are formed at the edge of drop panels, indicating that the drop
387 panels of WD-100 and WD-70 lose its efficiency for preventing punching shear failure at slab-

388 column connections. Therefore, the thickness of drop panel should be increased proportionately with
389 the increase of the slab thickness to ensure its efficiency.

390 For ND-series, similar to WD-series, specimen with a thicker slab has a greater FPL and lower
391 deformation capacity, as shown in Fig. 27(b). The FPL of ND-100 is larger than that of ND-70 and
392 ND-50 by 84.0 % and 197.8 %. Moreover, punching shear failure was observed in ND-100 before
393 reaching its yield load. Conversely, punching shear failure was observed after reaching their yield
394 load for ND-70 and ND-55, which indicates that the failure mode prone to brittle punching shear
395 failure with increasing the slab thickness.

396 **6. Conclusions**

397 Following conclusions can be made through the studies presented in this paper:

- 398 1. The numerical models built by LS-DYNA are able to simulate the structural behavior of RC flat
399 slab substructures subjected to a middle column missing scenario under quasi-static loading
400 regime well. The CSCM employed in the model can effectively predict the punching shear
401 failure at slab-column connections.
- 402 2. Numerical analysis on different boundary conditions at the overhang edge indicates that using
403 fixed constraints at the slab edges may over-estimate the response, while only rigid horizontal
404 constraints at the overhang edge are more realistic.
- 405 3. The numerical results indicated in numerical or experimental studies, only considering first
406 storey or including upper stories does not alter the response of the first floor greatly. However,
407 the load resistance from each story in a multi-storey building is different. This is because the
408 interaction among the stories causes different in-plane force developed in each story, which
409 influences the mobilization of membrane actions (CMA and TMA).
- 410 4. Increasing the integrity reinforcement ratio can increase the yield load, first peak load, and
411 second peak load of the specimens, especially for second peak load. The numerical results
412 indicate that the minimum integrity reinforcement ratio is suggested to be 0.63 % to ensure good
413 post-punching performance of the flat slab substructure to resist progressive collapse.

414 5. For RC flat slab structure under uniformly distributed load condition increasing the slab
415 thickness could significantly increase the first peak load while reduce the deformation capacity
416 remarkable. This is because the slab thickness has little effects on the residual load resisting
417 capacity at large deformation stage after column removal.

418 **7. Acknowledgements**

419 This research was supported by a research grant provided by the Natural Science Foundation of
420 China (Nos.51778153, 51568004, 51478118). Any opinions, findings and conclusions expressed in
421 this paper do not necessarily reflect the view of Natural Science Foundation of China.

422

423

424 **References**

- 425 [1] Department of Defense (DoD). Design of building to resist progressive collapse. Unified Facility
426 Criteria, UFC 4-023-03. Washington (DC): US Department of Defense, 2009.
- 427 [2] GSA. Progressive collapse analysis and design guidelines for new federal office buildings and
428 major modernization projects. U.S. General Service Administration, 2003, Washington, DC.
- 429 [3] ASCE/SEI 7. Recommendations for designing collapse-resistant structures. Structural
430 Engineering Institute-American Society of Civil Engineers, 2010, Reston, VA.
- 431 [4] COST Action TU0601. Robustness of structures. Proceedings of the 1st Workshop. ETH Zurich:
432 European Cooperation in Science and Technology, 2008.
- 433 [5] Y.P. Su, Y. Tian, X.S. Song, Progressive collapse resistance of axially-restrained frame beams,
434 *ACI Struct. J.* 106(5) (2009) 600-607.
- 435 [6] J. Yu, K.H. Tan, Experimental and numerical investigation on progressive collapse resistance of
436 reinforced concrete beam column sub-assemblages, *Eng. Struct.* 55 (2013) 90-106.
- 437 [7] D.C. Feng, Z. Wang, G. Wu, Progressive collapse performance analysis of precast reinforced
438 concrete structures, *Struct. Design Tall Spec. Build.* 28 (2019).
- 439 [8] A. Fascetti, S.K. Kunnath, N. Nistico, Robustness evaluation of RC frame buildings to
440 progressive collapse, *Eng. Struct.* 86 (2015) 242-249.
- 441 [9] E. Livingston, M. Sasani, M. Bazan, S. Sagiroglu, Progressive collapse resistance of RC beams,
442 *Eng. Struct.* 95 (2015) 61-70.
- 443 [10] J. Yu, L.Z. Luo, Y. Li, Numerical study of progressive collapse resistance of RC beam-slab
444 substructures under perimeter column removal scenario, *Eng. Struct.* 159 (2018) 14-27.
- 445 [11] S.D. Shan, S. Li, S.Y. Xu, L.L. Xie, Experimental study on the progressive collapse performance
446 of RC frames with infill walls, *Eng. Struct.* 111 (2016) 80-92.

- 447 [12] F. Sadek, J. Main, H. Lew, Y. Bao, Testing and analysis of steel and concrete beam-column
448 assemblies under a column removal scenario, *J. Struct. Eng.* 137(9) (2011) 881-892.
- 449 [13] K. Qian, B. Li, Slab effects on response of reinforced concrete substructures after loss of corner
450 column, *ACI Struct. J.* 109 (6) (2012) 845-855.
- 451 [14] A.T. Pham, N.S. Lim, K.H. Tan, Investigations of tensile membrane action in beam-slab systems
452 under progressive collapse subject to different loading configurations and boundary conditions,
453 *Eng. Struct.* 150 (2017) 520-536.
- 454 [15] X.Z. Lu, K.Q. Lin, Y. Li, H. Guan, P.Q. Ren, Y.L. Zhou, Experimental investigation of RC
455 beam-slab substructures against progressive collapse subject to an edge-column-removal
456 scenario, *Eng. Struct.* 149 (2017) 91-103.
- 457 [16] P.Q. Ren, Y. Li, X.Z. Lu, H. Guan, Y.L. Zhou, Experimental investigation of progressive
458 collapse resistance of one-way reinforced concrete beam-slab substructures under a middle-
459 column-removal scenario, *Eng. Struct.* 118 (2016) 28–40.
- 460 [17] D.C. Feng, S.C. Xie, W.N. Deng, Z.D. Ding, Probabilistic failure analysis of reinforced concrete
461 beam-column sub-assembly under column removal Scenario, *Eng. Fail. Anal.* 100 (2019) 381-
462 392.
- 463 [18] J.M. Russell, J.S. Owen, I. Hajirasouliha, Experimental investigation on the dynamic response of
464 RC flat slabs after a sudden column loss, *Eng. Struct.* 99 (2015) 28-41.
- 465 [19] K. Qian, B. Li, Resilience of flat slab structures in different phases of progressive collapse, *ACI*
466 *Struct. J.* 113(3) (2015) 537-548.
- 467 [20] K. Qian, B. Li, Load-resisting mechanism to mitigate progressive collapse of flat slab structures,
468 *Mag. Concr. Res.* 67(7) (2015) 349-363.
- 469 [21] F. H. Ma, B. P. Gilbert, H. Guan, H. Z. Xue, X. Z. Lu, Y. Li, Experimental study on the
470 progressive collapse behavior of RC flat plate substructures subjected to corner column removal
471 scenarios, *Engineering Structures*, 180 (2019) 728-741.
- 472 [22] L. Keyvani, M. Sasani, Y. Mirzaei, Compressive membrane action in progressive collapse
473 resistance of RC flat plates, *Eng. Struct.* 59 (2014) 554-564.
- 474 [23] R.J. Liu, Y. Tian, S.L. Orton, A.M. Said, Resistance of flat-plate buildings against progressive
475 collapse. I: modeling of slab-column connections, *J. Struct. Eng.* 141(12) (2014) 04015053.
- 476 [24] Z.H. Peng, S.L. Orton, J.R. Liu, Y. Tian, Experimental study of dynamic progressive collapse in
477 flat-plate buildings subjected to exterior column removal, *J. Struct. Eng.* 143(9) (2017) 04017125.
- 478 [25] K. Qian, Y.H. Weng, B. Li, Impact of two columns missing on dynamic response of RC flat slab
479 structures, *Eng. Struct.* 177 (2018) 598-615.
- 480 [26] ACI Committee 318. Building code requirements for structural concrete (ACI 318-11) and
481 commentary (318R-11). American Concrete Institute, 2011, Farmington Hills, MI, p. 433.

- 482 [27] J. Hallquist, LS-DYNA keyword user's manual, Version 971, Livermore Software Technology
483 Corp., 2007, Livermore, CA.
- 484 [28] J. Yu, Y.P. Gan, J. Wu, H. Wu, Effect of concrete masonry infill walls on progressive collapse
485 performance of reinforced concrete infilled frames, Eng. Struct. 191 (2019) 179-193.
- 486 [29] A.T. Pham, K.H. Tan, J. Yu, Numerical investigations on static and dynamic responses of
487 reinforced concrete sub-assemblages under progressive collapse, Eng. Struct. 149 (2017) 2-20.
- 488 [30] Y. Wu, J.E. Crawford, J.M. Magallanes, Performance of LS-DYNA concrete constitutive models,
489 12th Int. LS-DYNA Users Conf., Livermore Software Technology Corporation, 2012, Livermore,
490 CA.
- 491 [31] CEB. CEB-FIP model code 1990. 1991, Thomas Telford.
- 492 [32] Z.H. Peng, S.L. Orton, J.R. Liu, Y. Tian, Effects of in-plane restraint on progression of collapse
493 in flat-plate structures, Journal of Performance of Constructed Facilities. 31(3) (2017) 04016112.
- 494
- 495

496 **Figure caption list**

- 497 **Fig. 1.** Dimension and reinforcement details of Specimen WD (unit: in mm)
- 498 **Fig. 2.** An overview of a specimen in position ready for testing
- 499 **Fig. 3.** The detailing of load distribution rig (Item 9 in Figure 2)
- 500 **Fig. 4.** Numerical model of Specimen WD
- 501 **Fig. 5.** Details of numerical model for load distribution rig
- 502 **Fig. 6.** Yield surface of CSCM model
- 503 **Fig. 7.** Unconfined uniaxial stress-strain relationship of concrete based on CSCM model
- 504 **Fig. 8.** Comparison of different mesh sizes
- 505 **Fig. 9.** Comparison of the load-displacement curves between simulation and test
- 506 **Fig. 10.** Comparison of crack pattern of ND from simulation and test
- 507 **Fig. 11.** Comparison of crack pattern of WD from simulation and test
- 508 **Fig. 12.** Failure mode of ND
- 509 **Fig. 13.** Failure mode of WD
- 510 **Fig. 14.** Different constrains of overhang edge
- 511 **Fig. 15.** Numerical model of ND-R
- 512 **Fig. 16.** Comparison of load-displacement curve of ND with varying constraints
- 513 **Fig. 17.** Numerical models of multi-story RC flat slab substructures
- 514 **Fig. 18.** Comparison of resistance in the first story of the multi-story RC flat slab substructures
- 515 **Fig. 19.** Numerical models of ND-3F-R
- 516 **Fig. 20.** Comparison of the load resistance of the first story from ND-1F and ND-3F-R

517 **Fig. 21.** Comparison of the load resistance from different stories
518 **Fig. 22.** Locations of slab sections
519 **Fig. 23.** Comparison of the in-plane force in x direction
520 **Fig. 24.** Comparison of ND with different number of integrity reinforcements
521 **Fig. 25.** Comparison of ND-R with different number of integrity reinforcements
522 **Fig. 26.** Failure mode of ND-R without integrity reinforcement
523 **Fig. 27.** Investigation on effects of slab thickness
524 **Fig. 28.** Failure modes of WD-70 and WD-100

525

526

527

528

529

530

531

532

533

534

535

536

537

538

539

540

541

542

543

544

545

546

547

548

549

550

551

552

553
554
555

Table 1. Specimen properties from Qian and Li [20]

Test	Elements				Slab Rebar		
	Interior Column stub	Edge or Corner Columns	Drop Panel Thickness	Drop Panel Rebar, mm	Slab Thickness	Top Layer, mm	Bottom Layer, mm
ND	Height=390 mm Cross-section=200×200 mm ²	Height=300 mm Cross-section=200×200 mm ² Reinforcement ratio=2.6%	N.A	N.A	55 mm	R6@250	R6@250
WD	Reinforcement ratio=1.3%		35 mm	R6@80	55 mm	R6@250	R6@250

556
557
558
559
560

Table 2. User-input parameters of CSCM (Units: N, mm and ms)

MID 1	RO 0.00232	NPLOT 1	INCRE 0.0	IRATE 0	ERODE 1.10	RECOV 0.0	ITRETRC 0
PRED 0							
G 10396.30	K 11386.43	ALPHA 13.2996	THETA 0.2734	LAMDA 10.5	BETA 0.01929	NH 0	CH 0
ALPHA1 0.74735	THETA1 0.001327	LAMDA1 0.17	BETA1 0.07680	ALPHA2 0.66	THETA2 0.001596	LAMDA2 0.16	BETA2 0.07680
R 5.0	XD 87.6	W 0.05	D1 2.5e-04	D2 3.492e-07			
B 100.0	GFC 3.7760	D 0.1	GFT 0.03776	GFS 0.01888	PWRC 5.0	PWRT 1.0	PMOD 0.0
ETA0C 0	NC 0	ETAOT 0	NT 0	OVERC 0	OVERT 0	SRATE 0	REPOW 0

561
562
563

Table 3. Sensitivity analysis on mesh size

Type	Mesh 1	Mesh 2	Mesh 3
Mesh size at flat slab (mm)	30 × 30 × 27.5	25 × 25 × 18.33	15 × 15 × 13.75
Mesh size at other parts (mm)	30 × 30 × 30	25 × 25 × 25	15 × 15 × 15
Length of beam element (mm)	30	30	15
Total number of solid elements	63,891	104,784	392,800
Total number of beam elements	9386	9386	21,550
Computing time (s)	8912	12,152	29,250

564
565
566
567
568
569
570
571
572
573
574
575

576
577
578

Table 4. Comparison of the key results between test specimens and FE models

Results Source	ND			WD		
	YL (kN)	FPL (kN)	ULC (kN)	YL (kN)	FPL (kN)	ULC (kN)
Test	134.3	180.8	206.3	185.6	241.5	251.3
FE	137.4	179.5	209.2	190.5	238.6	235.4
FE/Test	1.02	0.99	1.01	1.03	0.99	0.94

Note: YL represents yield load; FPL represents first peak load; ULC represents ultimate load capacity.

579
580
581
582
583

Table 5. Key results of ND with different amount of integrity reinforcement

Amount (ρ_i %)	YL (kN)	FPL (kN)	SPL (kN)	Disp. of SPL (mm)
None	118.5	147.9	82.3	104.1
1R6 (0.31)	122.6	154.6	123.9	164.1
2R6 (0.63)	126.8	171.7	179.8	154.0
3R6 (0.94)	137.4	179.5	209.2	140.4
4R6 (1.26)	138.2	191.7	224.1	139.9
5R6 (1.57)	138.8	196.9	240.3	123.2
6R6 (1.88)	140.4	209.4	254.6	115.3

Note: YL represents yield load; FPL represents first peak load; SPL represents second peak load.

584
585
586
587
588
589
590
591
592
593
594
595
596
597
598
599
600
601
602
603
604
605
606
607
608
609
610
611
612
613
614
615
616
617
618
619
620
621
622

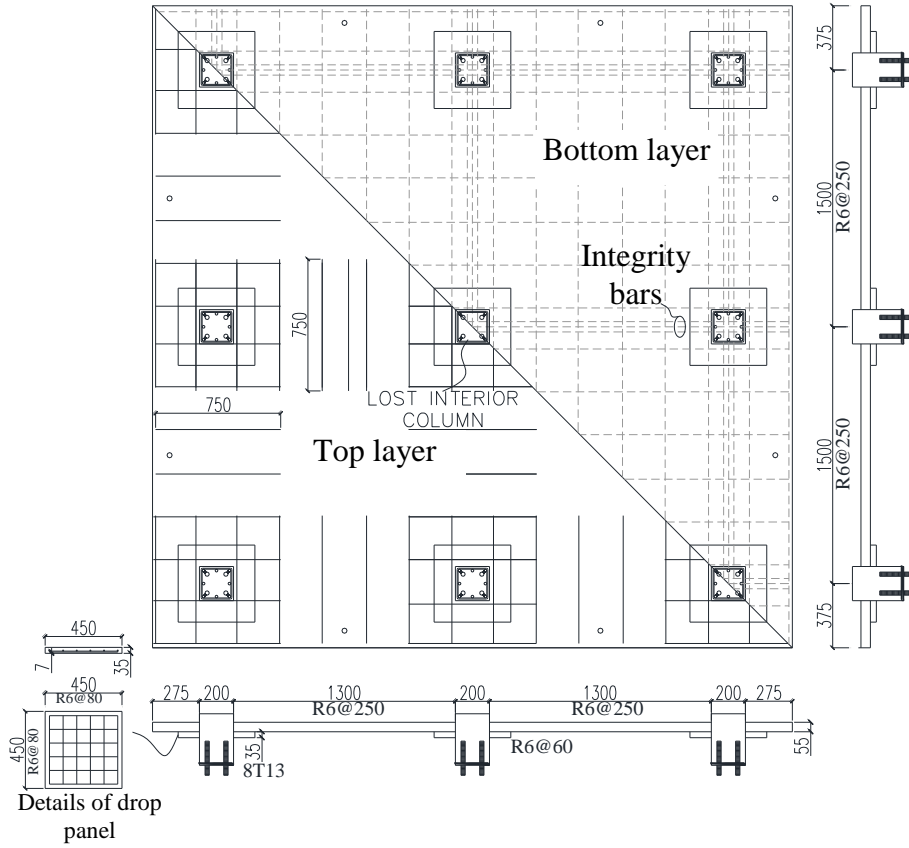
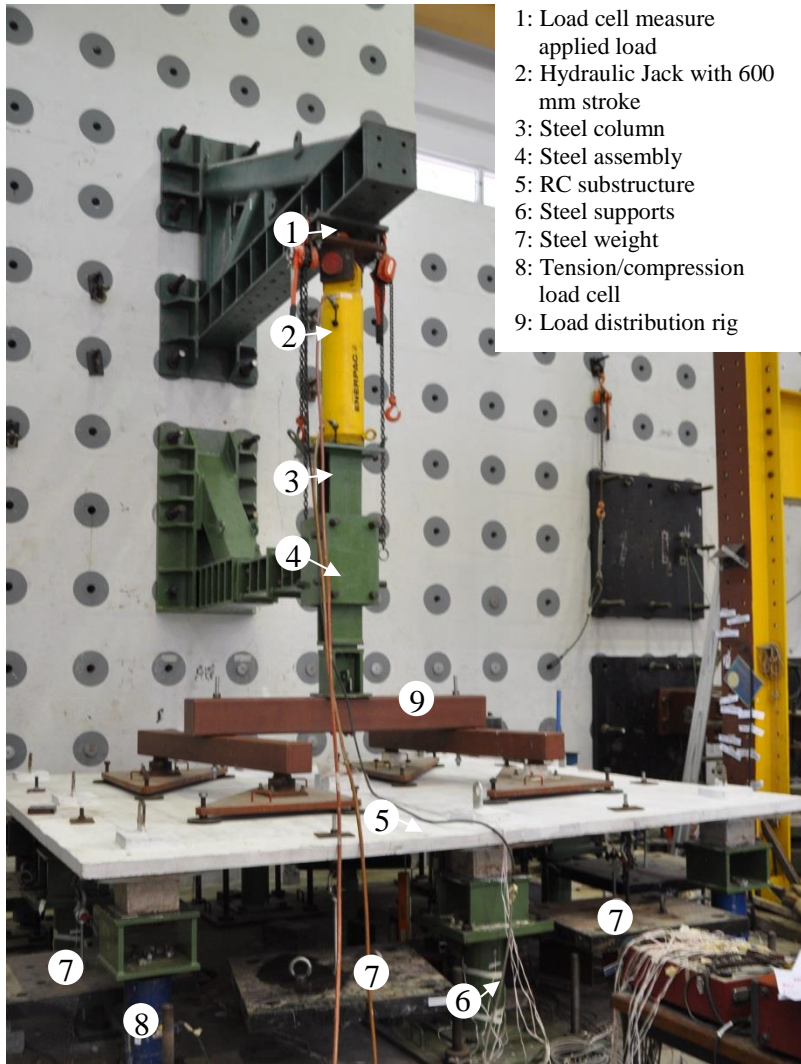


Fig. 1. Dimension and reinforcement details of Specimen WD (unit: in mm)

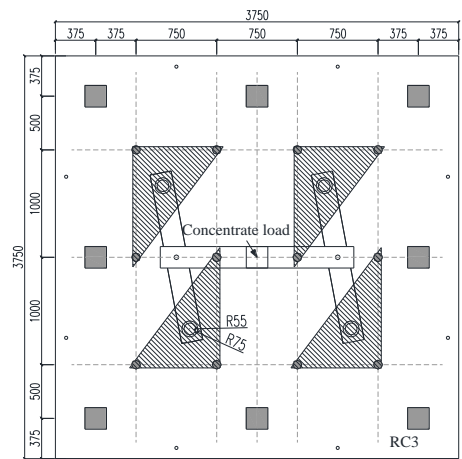
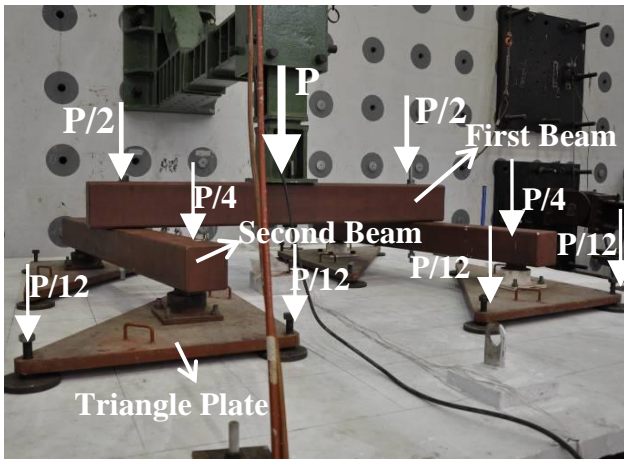
624
 625
 626
 627
 628
 629
 630
 631
 632
 633
 634
 635
 636
 637
 638
 639
 640
 641
 642
 643
 644
 645
 646
 647
 648
 649
 650
 651
 652
 653
 654



- 1: Load cell measure applied load
- 2: Hydraulic Jack with 600 mm stroke
- 3: Steel column
- 4: Steel assembly
- 5: RC substructure
- 6: Steel supports
- 7: Steel weight
- 8: Tension/compression load cell
- 9: Load distribution rig

Fig. 2. An overview of a specimen in position ready for testing

655
656
657
658
659
660



(a) Schematic of the load distribution

(b) Arrangement of the twelve loading points

Fig. 3. The detailing of load distribution rig (Item 9 in Figure 2)

661
662
663
664

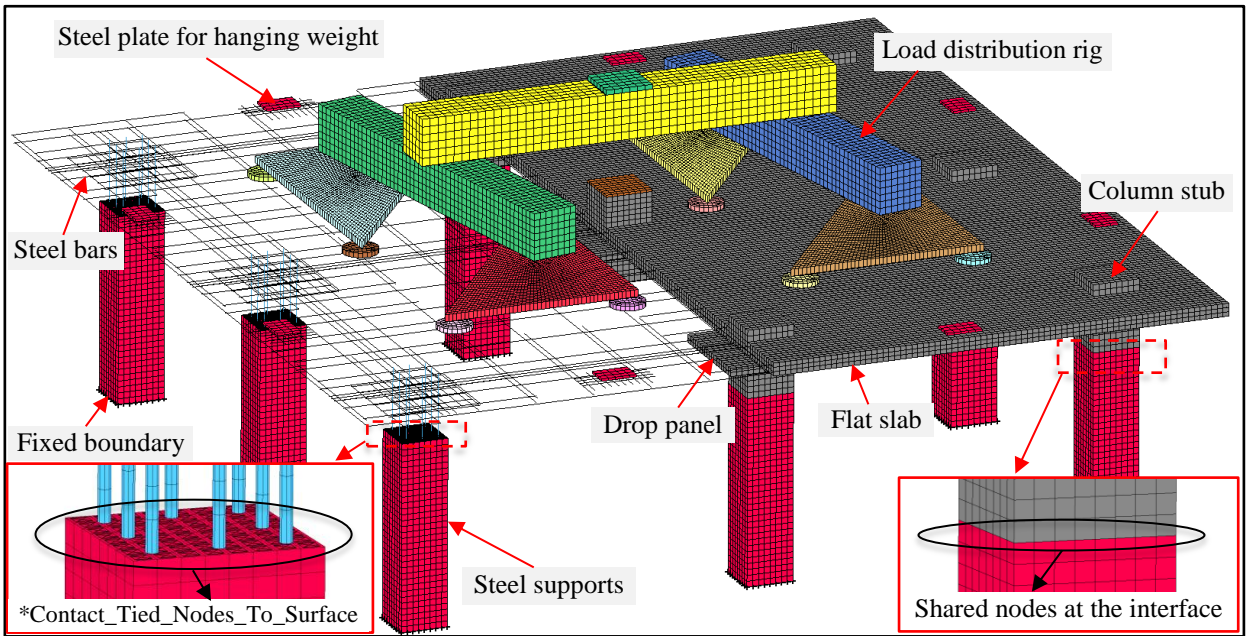


Fig. 4. Numerical model of Specimen WD

665
666
667

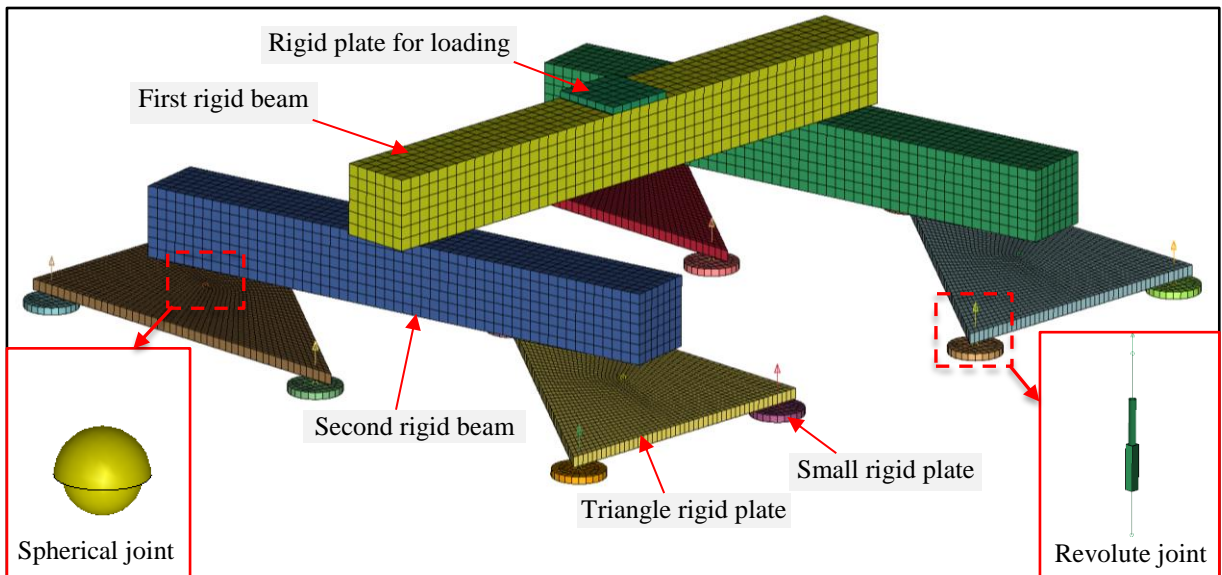


Fig. 5. Details of numerical model for load distribution rig

668
669
670

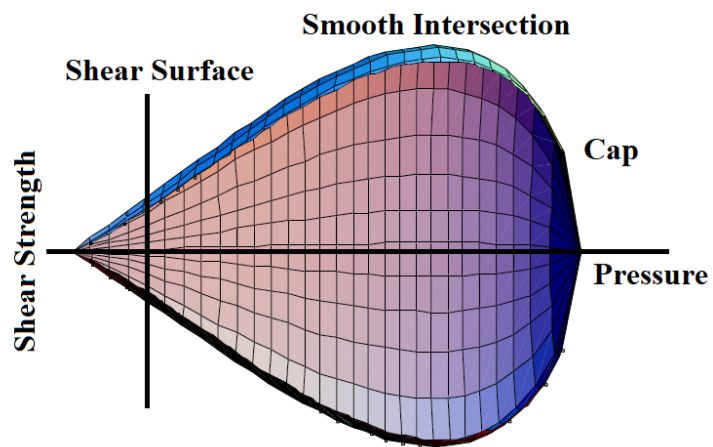
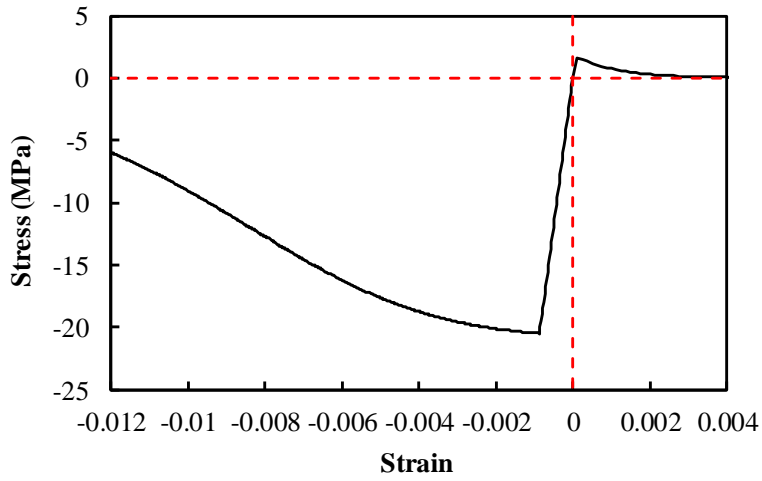
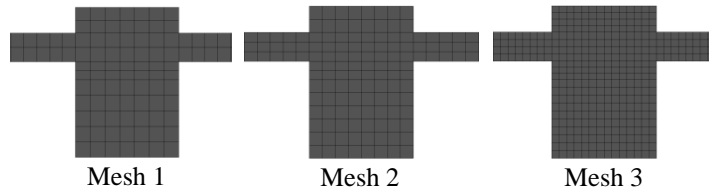
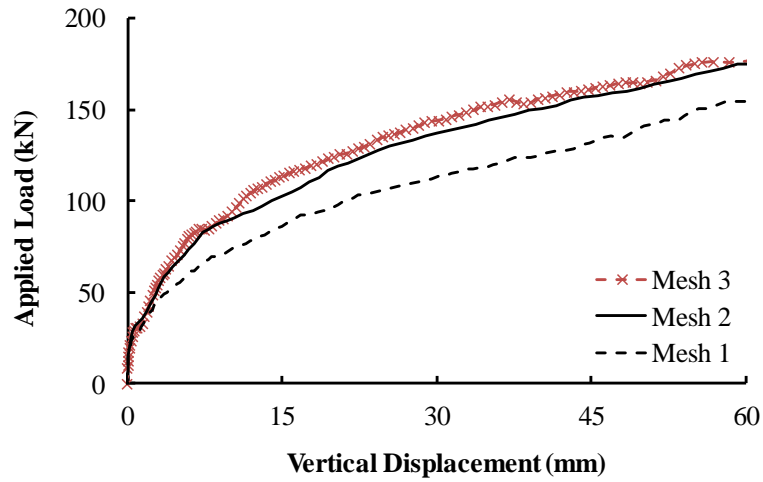


Fig. 6. Yield surface of CSCM model

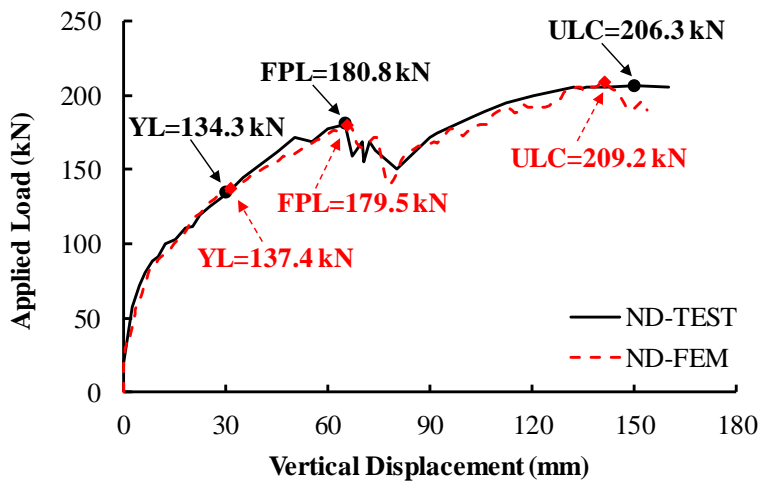
671
672
673
674



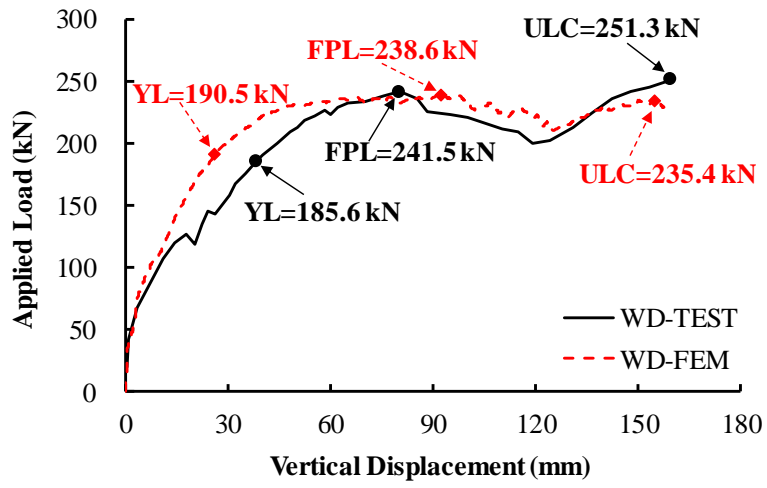
675
676
677
Fig. 7. Unconfined uniaxial stress-strain relationship of concrete based on CSCM model



678
679
680
Fig. 8. Comparison of different mesh sizes

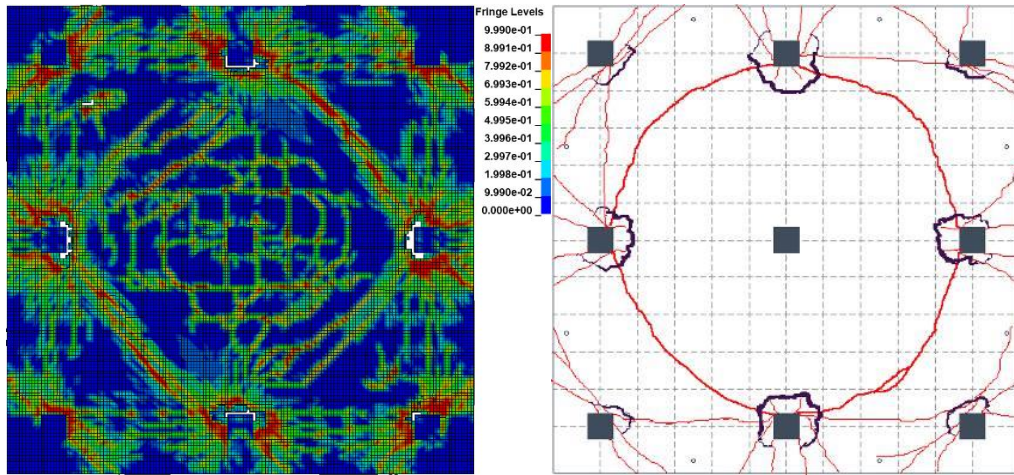


681
682
(a) ND

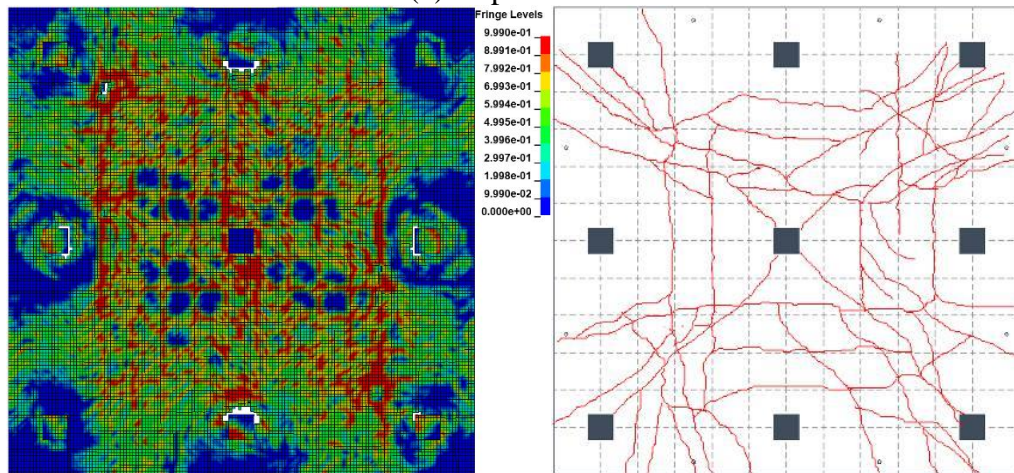


(b) WD

Fig. 9. Comparison of the load-displacement curves between simulation and test



(a) Top view



(b) Bottom view

Fig. 10. Comparison of crack pattern of ND from simulation and test

683

684

685

686

687

688

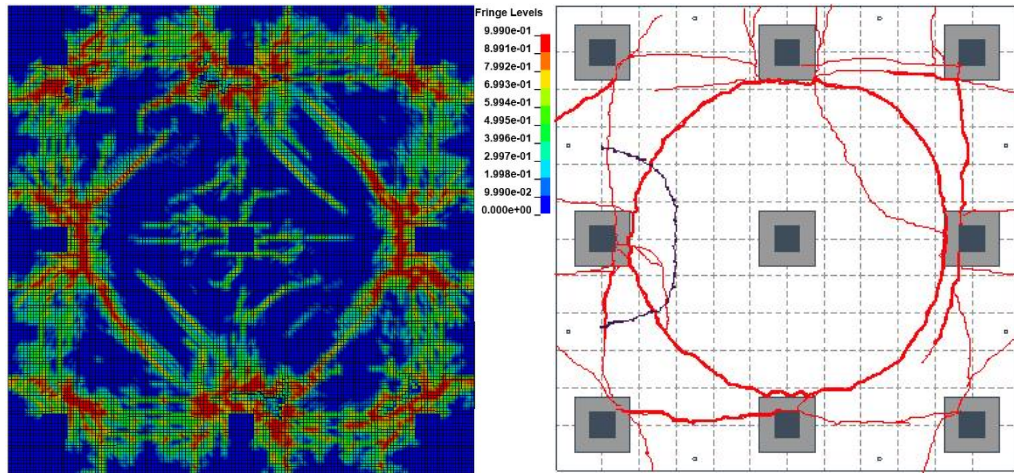
689

690

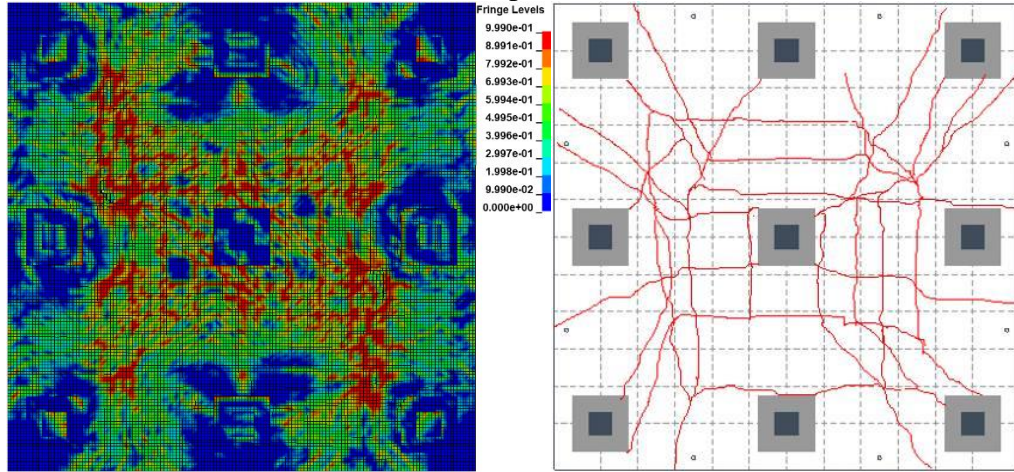
691

692

693
694



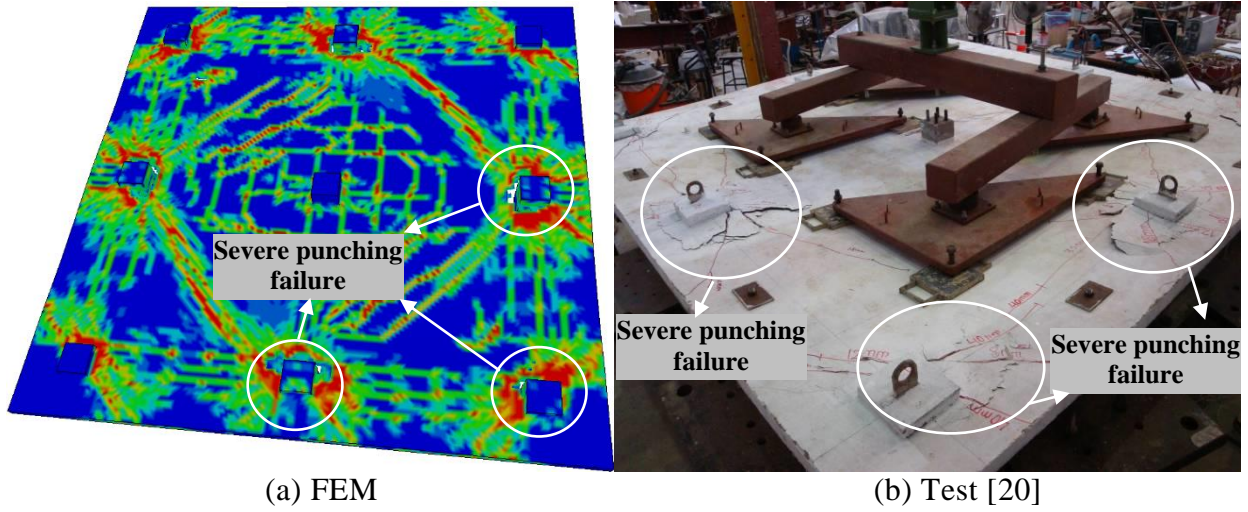
(a) Top view



(b) Bottom view

Fig. 11. Comparison of crack pattern of WD from simulation and test

695
696
697
698



(a) FEM

(b) Test [20]

Fig. 12. Failure mode of ND

699
700
701
702
703
704
705
706
707
708
709
710

711
712

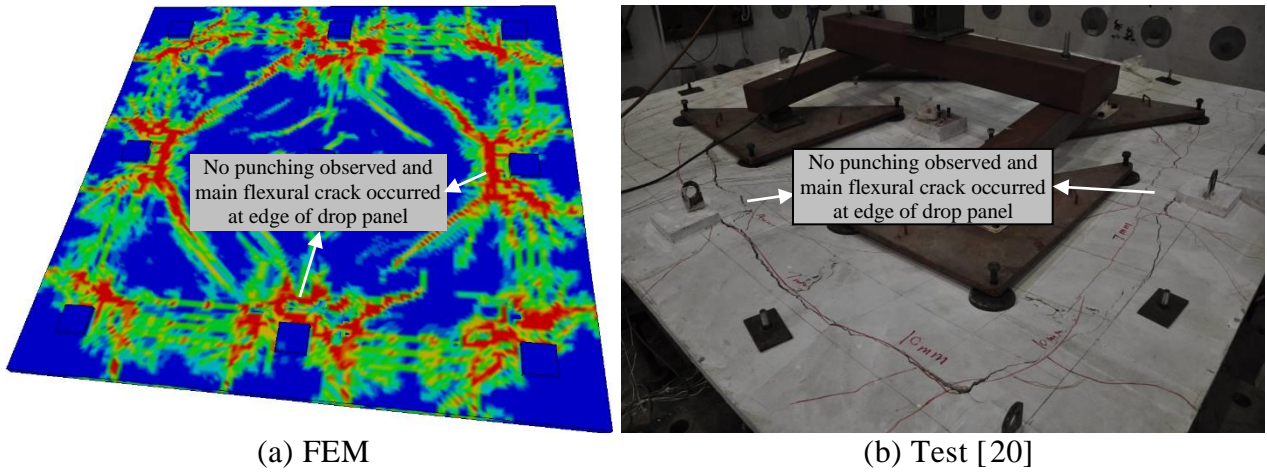
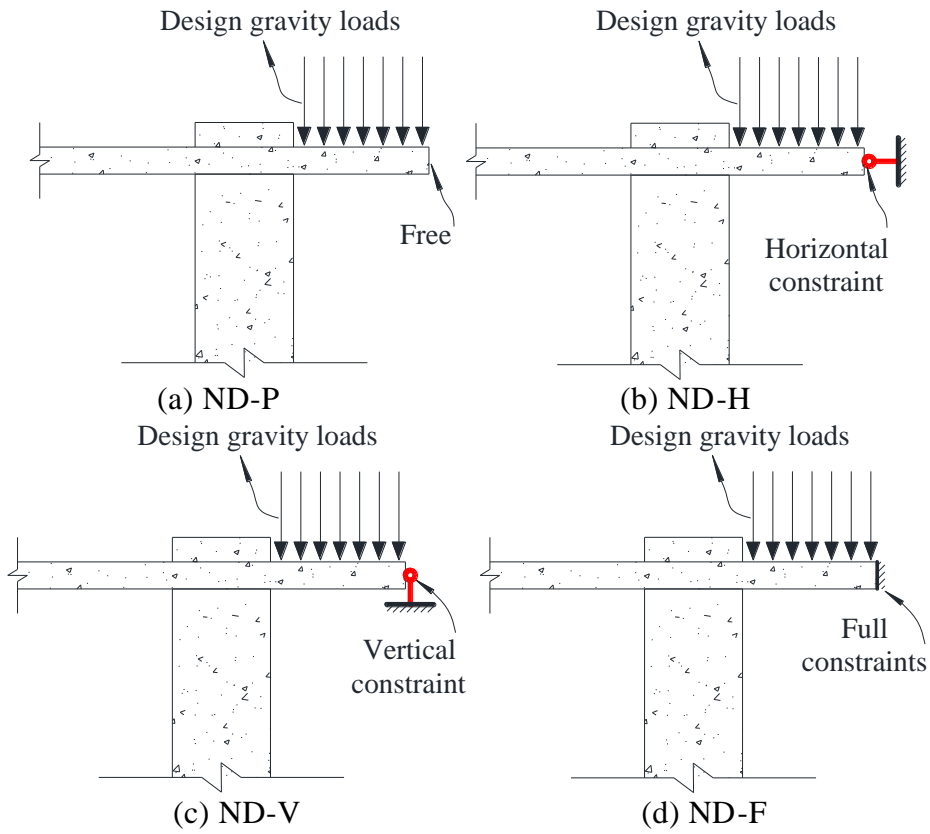


Fig. 13. Failure mode of WD

713
714
715
716
717
718
719
720
721

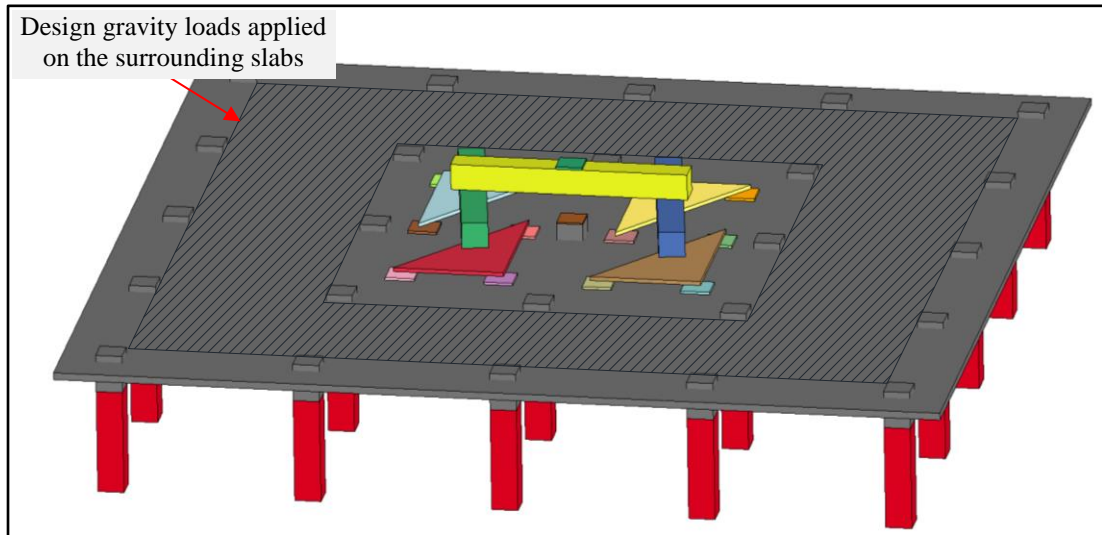


722
723

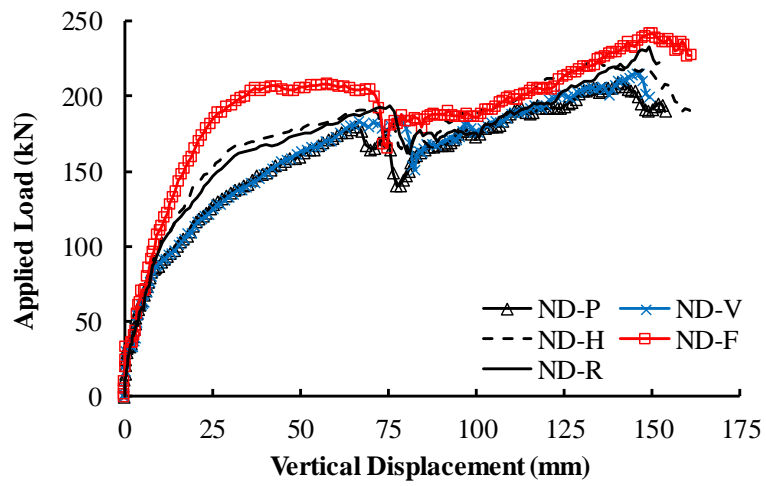
724
725
726
727
728
729
730
731
732
733
734

Fig. 14. Different constrains of overhang edge

735
736

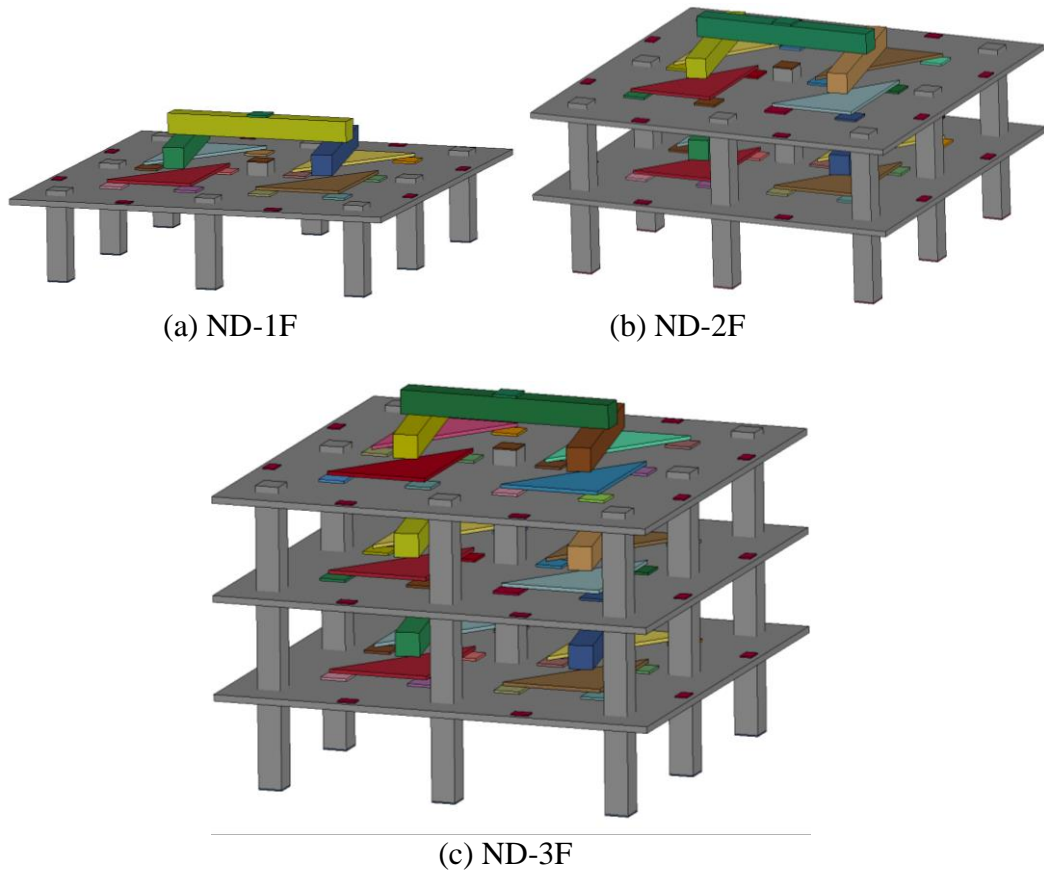


737
738
739
740
741
742
743
Fig. 15. Numerical model of ND-R



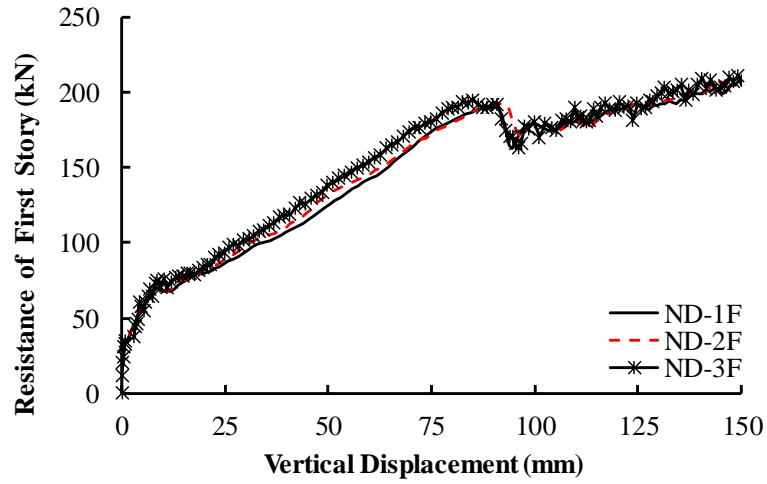
744
745
746
747
748
749
750
751
752
753
754
755
Fig. 16. Comparison of load-displacement curve of ND with varying constraints

756
757
758



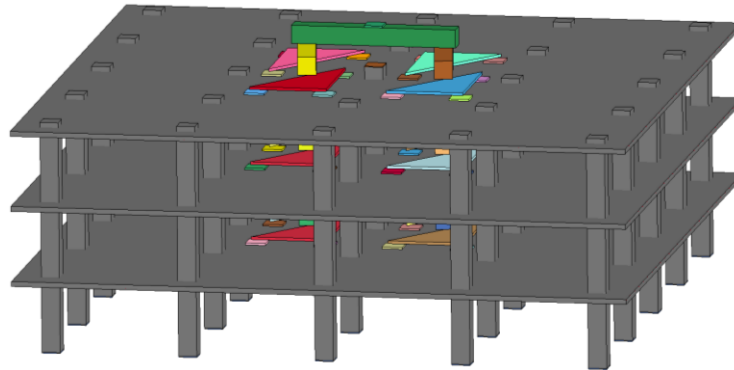
759
760
761

Fig. 17. Numerical models of multi-story RC flat slab substructures



762
763

Fig. 18. Comparison of resistance in the first story of the multi-story RC flat slab substructures



764
765
766
767
768

769
770
771

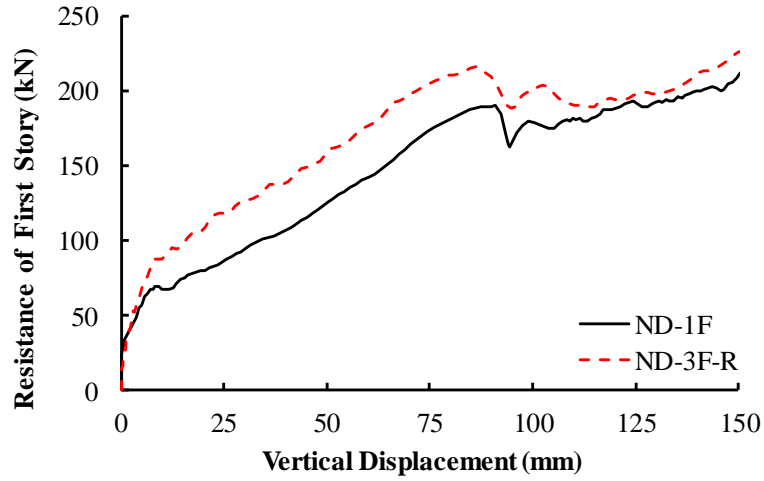
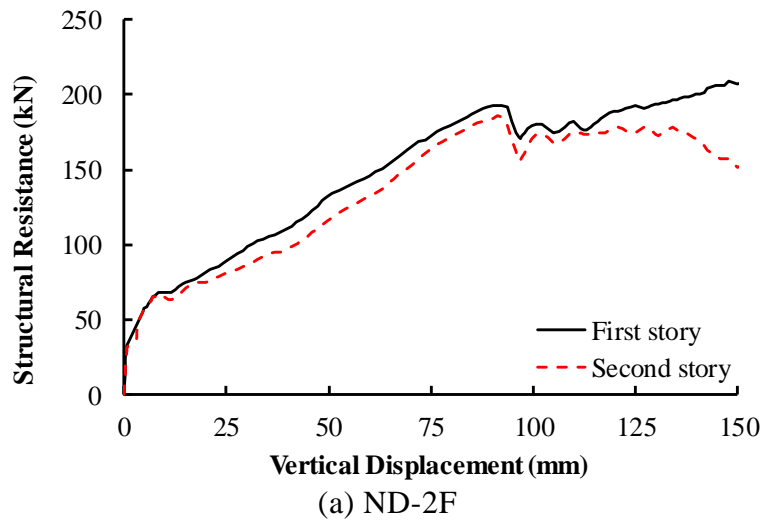


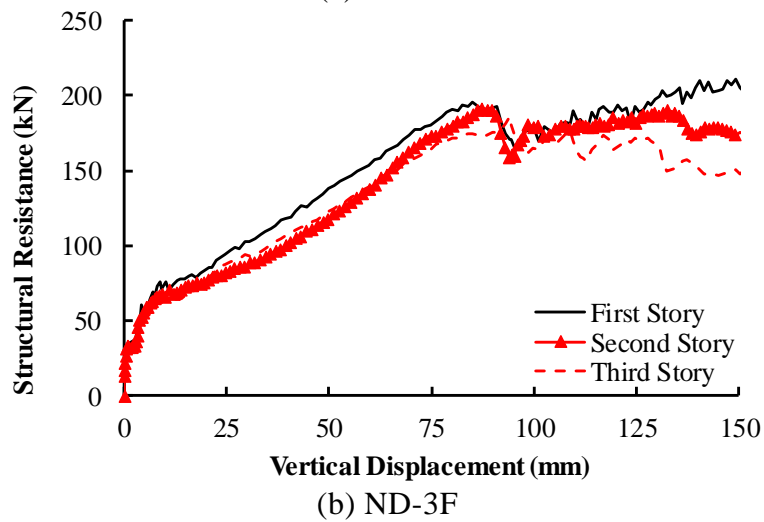
Fig. 20. Comparison of the load resistance of the first story from ND-1F and ND-3F-R

772
773
774
775



(a) ND-2F

776
777



(b) ND-3F

778
779

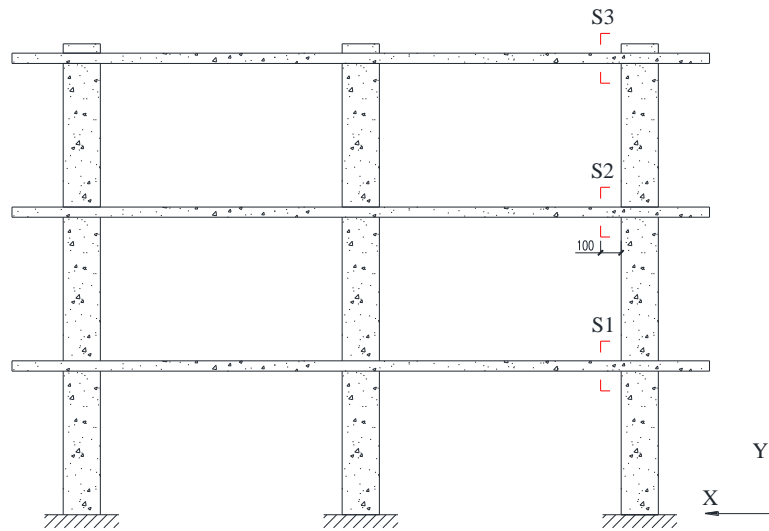
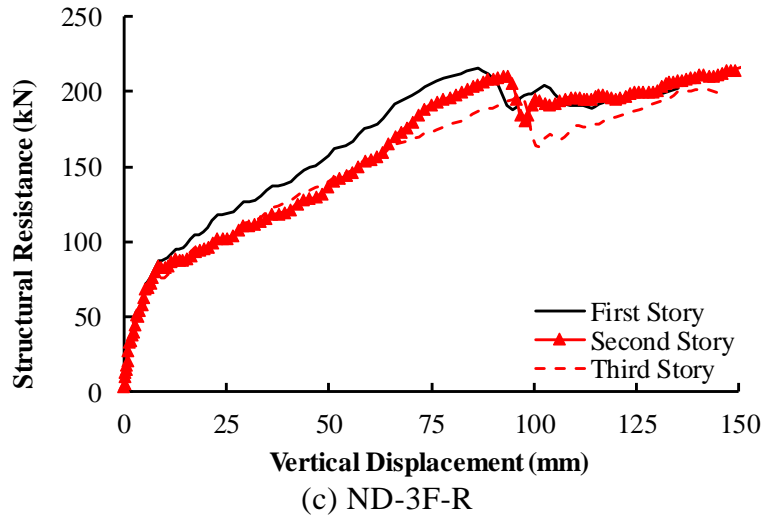


Fig. 22. Locations of slab sections

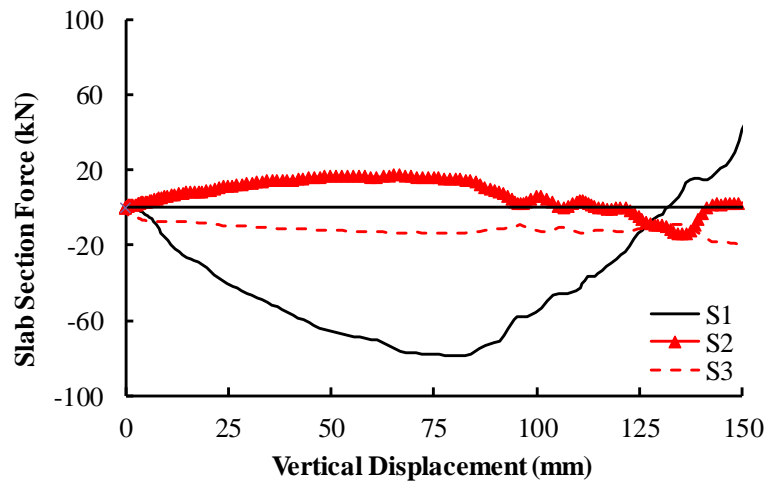
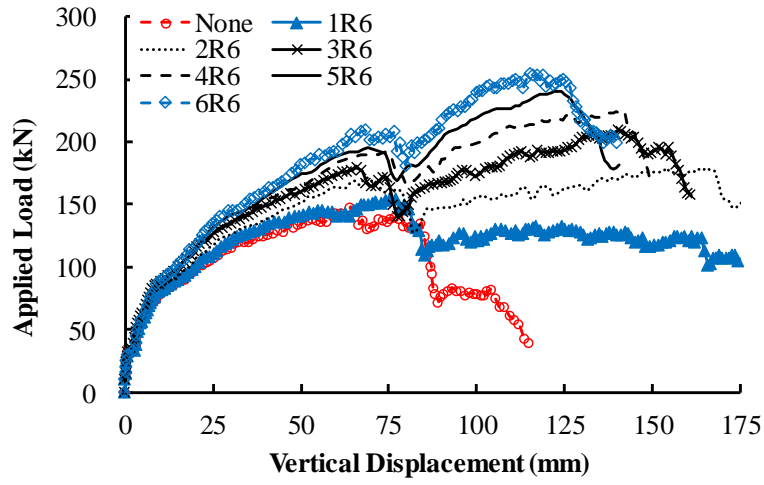
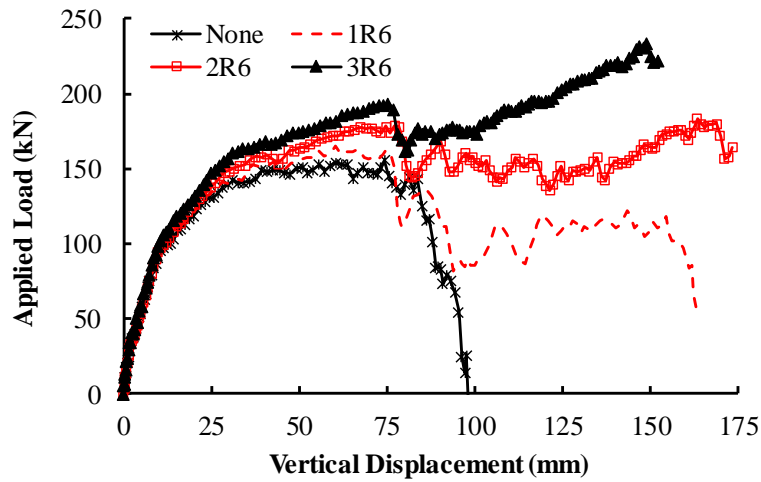


Fig. 23. Comparison of the in-plane force in x direction



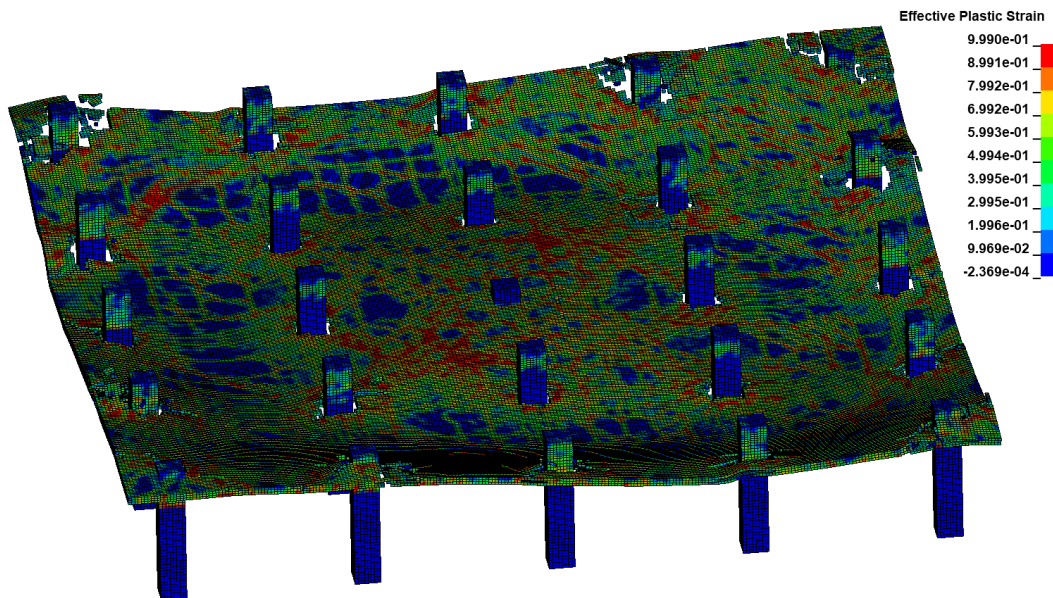
790
791
792

Fig. 24. Comparison of ND with different number of integrity reinforcements



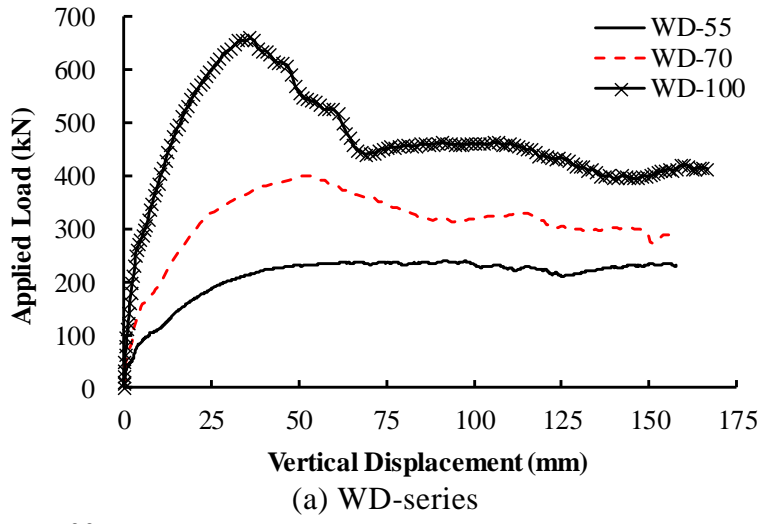
793
794
795

Fig. 25. Comparison of ND-R with different number of integrity reinforcements

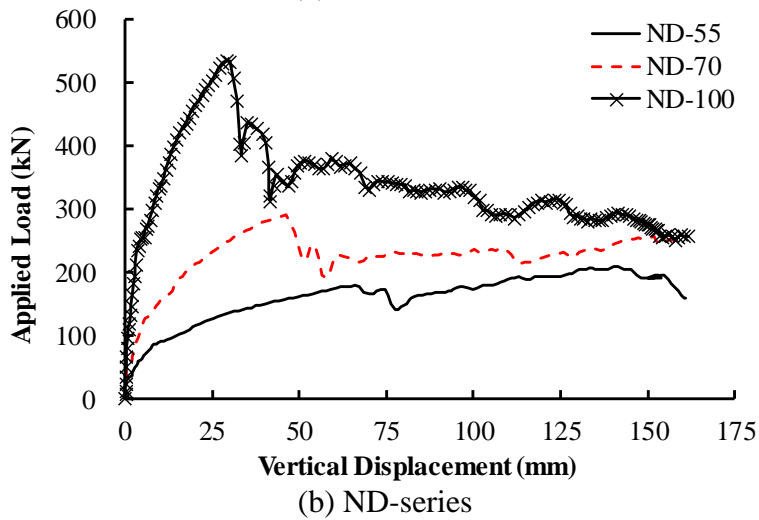


796
797
798
799

Fig. 26. Failure mode of ND-R without integrity reinforcement

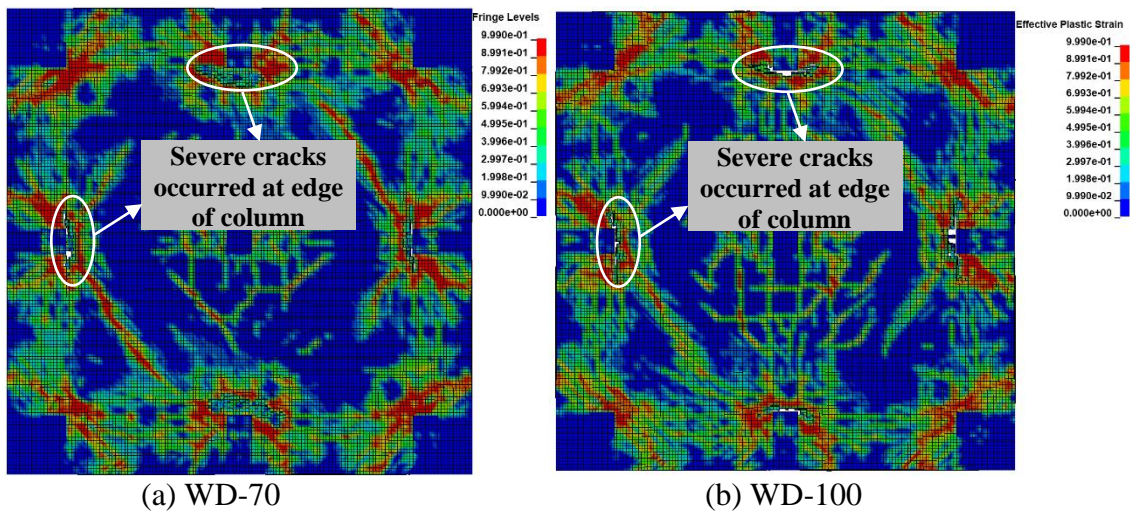


800
801



802
803
804
805

Fig. 27. Investigation on effects of slab thickness



806
807
808

Fig. 28. Failure modes of WD-70 and WD-100